

Quinacridone on Ag(111): Hydrogen Bonding versus Chirality

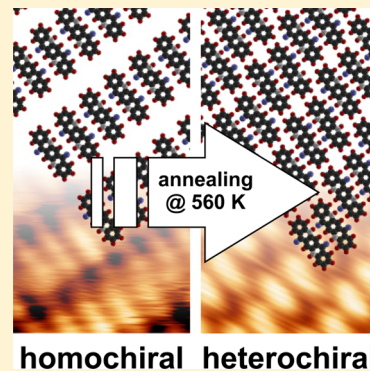
Thorsten Wagner,^{*,†} Michael Györök,[†] Daniel Huber,[†] Peter Zeppenfeld,[†] and Eric Daniel Glowacki[‡]

[†]Institute of Experimental Physics, Johannes Kepler University Linz, Altenberger Str. 69, 4040 Linz, Austria

[‡]Linz Institute for Organic Solar Cells (LIOS), Johannes Kepler University Linz, Altenberger Str. 69, 4040 Linz, Austria

Supporting Information

ABSTRACT: Quinacridone (QA) has recently gained attention as an organic semiconductor with unexpectedly high performance in organic devices. The strong intermolecular connection via hydrogen bonds is expected to promote good structural order. When deposited on a substrate, another relevant factor comes into play, namely the 2D-chirality of the quinacridone molecules adsorbed on a surface. Scanning tunneling microscopy (STM) images of monolayer quinacridone on Ag(111) deposited at room temperature reveal the formation of quasi-one-dimensional rows of parallel quinacridone molecules. These rows are segmented into short stacks of a few molecules in which adjacent, flat-lying molecules of a single handedness are linked via hydrogen bonds. After annealing to a temperature of $T = 550\text{--}570\text{ K}$, which is close to the sublimation temperature of bulk quinacridone, the structure changes into a stacking of heterochiral quinacridone dimers with a markedly different intermolecular arrangement. Electron diffraction (LEED) and photoelectron emission microscopy (PEEM) data corroborate the STM findings. These results illustrate how the effects of hydrogen bonding and chirality can compete and give rise to very different (meta)stable structures of quinacridone on surfaces.



INTRODUCTION

An extended π -conjugated system is generally considered to be a prerequisite for high electron mobility and, consequently, a good performance in organic thin film devices. Pentacene and rubrene are typical examples of this class of molecules. From the point of view of mesomeric structures, 5,12-dihydro-*quino[2,3-*b*]*acridine-7,14-dione—shortly called quinacridone (QA)—is a molecule with limited intramolecular π -conjugation, as resonance contributions of enol/imine mesomers are small. Such molecules are thus regarded to be poor candidates for organic semiconductors. The recent work of Glowacki et al. advances that this view may require revision: In their recent publications they illustrate the potential of quinacridone as functional material in organic field effect transistors (OFETs) and photovoltaics (PV).^{1–3} The authors were able to achieve field effect mobilities larger than $0.1\text{ cm}^2/(\text{Vs})$ and photocurrents in the mA/cm^2 range under simulated solar illumination. The surprisingly high mobility is attributed to strong intermolecular interactions via hydrogen bonds reinforcing π -stacking and crystalline ordering.

Quinacridone is a widely used organic pigment (Violet 19, $C_{20}\text{H}_{12}\text{N}_2\text{O}_2$, see inset of Figure 2 for its structural formula), which is industrially produced in large amounts and at low costs. Its atomic skeleton consists of five rings. It is perhaps best-known as constituting the magenta colorant for printer toners.^{4–6} In contrast to the well-known pentacene, its intramolecular conjugation is broken. Besides van der Waals interactions, intermolecular hydrogen bonds are most crucial for its crystalline structure. The polymorphs of the bulk material can be divided into two groups. In the α and β phase, quinacridone forms flat rows of parallelly arranged molecules.

This allows each quinacridone molecule to form two hydrogen bonds with both adjacent neighbors in the row. Therefore, these are known as the linear-chain polymorphs. In contrast, the γ polymorph exhibits a criss-cross arrangement so that each molecule is connected by one hydrogen bond to each of its four neighbors (for details on the bulk polymorphs, see refs 7–9). Theoretical investigations by Gao et al. predict that the hole mobility differs by a factor 100 between the α^I ($4.44 \times 10^{-1}\text{ cm}^2/(\text{V s})$) and the γ ($4.18 \times 10^{-3}\text{ cm}^2/(\text{V s})$) polymorph.¹⁰

In epitaxial thin films, one also has to consider the orientation of the crystallites, i.e., which lattice plane is parallel to the substrate surface. Depending on the crystallographic alignment, the long axis of rodlike molecules will adopt an upright standing or a flat-lying geometry on the surface. Since the highest mobility is generally obtained along the π -stacking direction, i.e., perpendicular to the long axis of the molecules, the orientation of the molecules on the substrate surface is essential for the functionality of a thin film device.¹¹ For an OFET, where the current flows parallel to the surface, an upright standing geometry is favored. In contrast, for an OLED or photovoltaic device where the charge transport and the emitted or incident light are directed perpendicular to the substrate surface, flat-lying molecules are preferred. Accordingly, Glowacki et al. have prepared quinacridone films with a “standing up” configuration on an aluminum oxide surface passivated by tetratetracontane to fabricate their OFETs.¹ On the other hand, adsorption of rodlike molecules on clean metal

Received: March 2, 2014

Revised: April 29, 2014

Published: May 1, 2014

surfaces generally adopt a flat-lying adsorption geometry due to the strong interaction of the molecules with the metal substrate. This is also the case for hydrogen-bonded molecules like 4-[*trans*-2-(pyrid-4-ylvinyl)]benzoic acid (PVBA) and 4-[{(pyrid-4-ylethynyl)}]benzoic acid (PEBA) on Ag(111)¹² or indigo on Cu(111)¹³ as well as for the adsorption of quinacridone on Ag(111) as will be reported below.

Finally, we want to stress the importance of 2D-chirality in the context of the adsorption of molecules (like quinacridone) on surfaces. Although chirality is a central and powerful concept in chemistry ever since its introduction by Pasteur, the notion of "surface chirality" and its fascinating consequences were explored only recently.^{14,15} For a 2D, prochiral molecule with a 3D inversion center like indigo or quinacridone, which is inclined with respect to a high symmetry direction of the surface, the 2D-mirror operation about this axis will leave the adsorption configuration unchanged but switch the handedness of the molecule on the surface. Therefore, the two adsorption configurations depicted in Figure 1 are the energetically

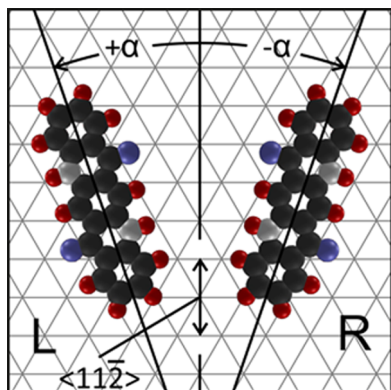


Figure 1. Schematic illustrating the relationship between the adsorption geometry of a quinacridone molecule and its 2D-chirality. In this example, the mirror plane is parallel to $\langle 11\bar{2} \rangle$ symmetry axis and normal to the surface. The atoms of the quinacridone are color coded as follows: carbon = gray, hydrogen = red, nitrogen = white, and oxygen = blue.

equivalent ones for the two different 2D-enantiomers.¹³ However, in its ground state, each of the two enantiomers adopts only one of the two mirror symmetric adsorption geometries, in particular either $-\alpha$ or $+\alpha$ according to its handedness. In the following, we will take advantage of this conjunction to differentiate between the two enantiomers of quinacridone molecules adsorbed on the Ag(111) surface.

EXPERIMENTAL SECTION

The experiments were carried out in an ultrahigh-vacuum system housing an Omicron VT AFM/STM, an Omicron low-energy electron diffraction optics (LEED), and a Focus photoelectron emission microscope (PEEM). The base pressure of the system was around 5×10^{-10} mbar. The Ag(111) single crystal was prepared by several cycles of sputtering with Ar⁺ ions (900 V, 4 μ A/cm² for 60 min) and subsequent annealing at 660 K. The quinacridone was purchased from TCI and purified by double temperature gradient sublimation in a vacuum of 5×10^{-7} mbar. The quinacridone was deposited while monitoring the photo-electron emission yield in the PEEM. During deposition, the quartz crucible with the quinacridone powder was held at 553

K while the sample was at room temperature. A Hg lamp (4.9 eV) was used as excitation source for the photoelectrons. A typical transient of the electron yield as a function of the deposition time is shown in Figure 2. We assume that the

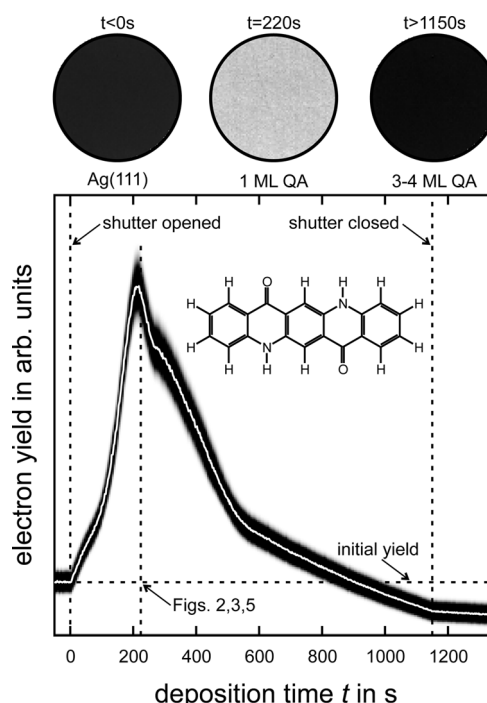


Figure 2. Representative PEEM images (top) and transient of the electron yield acquired during deposition of quinacridone on the Ag(111) surface (bottom). The white line shows the transient of the mean electron yield (averaged over the entire field of view of 80 μ m). The dark ribbon behind the white line arises from vertical "error bars", each of which is actually a complete histogram of the electron yield sampled over the entire field of view. The color ranges from white (low probability for the given electron yield) to black (high probability). In other words, the width of the dark ribbon is a measure for the variation of the electron yield across the PEEM image recorded at a given time t . In total, the ribbon shows the histograms of 702 images recorded during the growth experiment. The time interval between subsequent images is 2 s. The inset shows a structural formula of the quinacridone molecule.

maximum of the electron yield corresponds to the completion of the first monolayer. In order to prepare a single monolayer of quinacridone, the deposition was stopped either after reaching the maximum of the electron yield or after the deposition of an equivalent of 4–5 times this amount. In the second case, the sample was heated to 550–570 K to desorb the excess molecules in the multilayer.

The STM and LEED measurements were carried out in the same vacuum vessel without breaking the vacuum. All images were acquired at room temperature. For the particular STM setup, the bias voltage is applied to the tip while the sample is grounded. The STM images were processed using the free software tools Gwyddion¹⁶ and WSxM.¹⁷ If not stated otherwise, only a background subtraction and an optimization of the contrast were applied to the STM data. In order to minimize the electron beam induced damage during LEED measurements, the sample was moved to a "fresh" position every time a LEED image was acquired. Although the LEED pattern usually vanished after a couple of seconds when exposing the organic thin film to the electron beam, we were

not able to detect any damaged molecules by STM. In the same way we can exclude that there is a significant decomposition of the molecules due to the light exposure in the PEEM.

RESULTS AND DISCUSSION

PEEM Measurements. To monitor the growth of quinacridone, sequences of PEEM images (movies) were recorded while the Ag(111) was exposed to quinacridone. During the deposition, no characteristic features with length scales larger than $0.1\text{ }\mu\text{m}$ were observed; i.e., the local electron yield was spatially homogeneous within the field of view varying between 80 and $145\text{ }\mu\text{m}$. Even after deposition of more than 10 monolayers of quinacridone, we did not observe any crystallites or any significant spatial heterogeneity. For other organic materials like α -sexithiophene (6T),^{18,19} *p*-sexiphenyl (6P),^{20,21} and perylene-3,4,9,10-tetracarboxylic dianhydride (PTCDA),²² Stranski–Krastanov growth is typically observed; i.e., after formation of a wetting layer the growth of 3D islands sets in. As in these cases the ionization potential, i.e., the binding energy of the HOMO level with respect to the vacuum level, is higher than the maximum photon energy supplied by the Hg lamp; 3D crystalline structures have a lower emission yield in the PEEM than the adjacent wetting layer and thus appear darker than the surrounding wetting layer. For the case of quinacridone films, the HOMO is located $\approx 5.4\text{ eV}$ below the vacuum level.³ As a consequence, we do not expect any photoelectron emission from a thick layer of quinacridone if a Hg lamp is used for photoelectron excitation. Indeed, the electron yield depicted in Figure 2 for the bare Ag(111) surface (deposition time $t = 0\text{ s}$) is higher than for the surface covered with about 4–5 monolayer of quinacridone (deposition time $t = 1150\text{ s}$). Since for Ag(111) work function values ϕ in the range between 4.3 and 4.8 eV are reported, the pristine Ag(111) surface should (and actually does) appear bright in the PEEM images.^{22–25} Obviously, the growth transient depicted in Figure 2 does not show a monotonous decrease of the electron yield but a maximum which can be attributed to the completion of the first monolayer of quinacridone. The physical background of this feature is the formation of an interface dipole during the deposition of the first monolayer.^{26,27} Subsequent layers deposited on top of this monolayer do not alter the metal–organic interface any further but lead to an attenuation of the electron yield due to inelastic scattering of the photoelectrons excited at the interface upon traversing the quinacridone layer. As a consequence, the emission yield steadily decreases after reaching its maximum at monolayer coverage.

Quinacridone Monolayer Prepared at RT. The sample surface shown in Figure 3 was prepared by thermal evaporation of quinacridone while the sample was held at room temperature. Once the maximum of the electron yield was reached in the PEEM transient (cf. Figure 2), the shutter of the evaporator was closed. Therefore, the coverage should be just above one monolayer (1 ML). Indeed, the STM micrograph in Figure 3 shows a close-packed layer of quinacridone molecules. The molecules form extended quasi-one-dimensional rows of molecules segmented into stacks of a few nanometers length. The molecular rows have distinct orientations inclined by about $\pm 11^\circ$ with respect to one of the three equivalent $\langle 11\bar{2} \rangle$ crystallographic axes of the substrate. Therefore, the two mirror domains combined with the three rotationally equivalent $\langle 11\bar{2} \rangle$ axes of the substrate give rise to a total of six possible orientations of the rows. The angle between two neighboring, mirror symmetric orientations is $2 \times 11^\circ = 22^\circ$, as indicated in

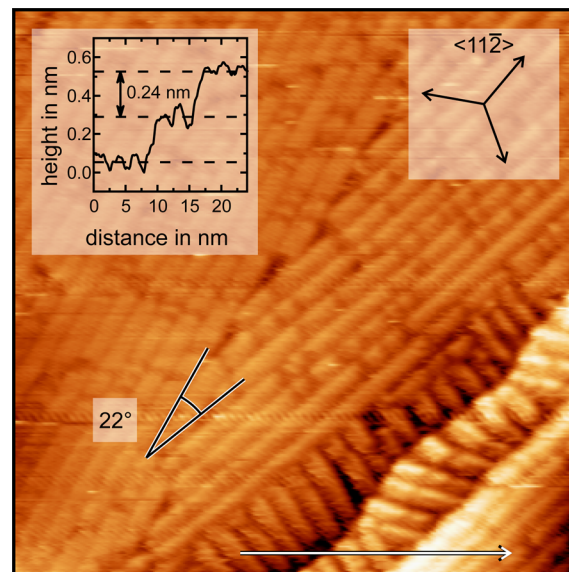


Figure 3. STM image of a close-packed monolayer of quinacridone on Ag(111) deposited while the sample was held at room temperature. The image has a size of $50 \times 50\text{ nm}^2$. The tunneling parameters were $U = 2\text{ V}$ and $I = 2\text{ pA}$. The white arrow at the bottom marks the position of the cross section displayed in the inset. The dashed lines indicate the expected step height of the Ag(111) substrate.

Figure 3. This is consistent with the LEED results discussed later on, which reveal that the molecular rows are aligned $\pm 10.9^\circ$ with respect to the $\langle 11\bar{2} \rangle$ directions of the substrate (see Figure 6).

Along the line profile indicated in Figure 3, two steps can be identified. Their height corresponds almost exactly to 0.24 nm , which is the expected step height on the Ag(111) surface. As no steps with other heights were observed, the coverage of quinacridone corresponds to just a single monolayer as expected from the PEEM transient in Figure 2. Excess molecules which might be present in the second layer on top of the quinacridone monolayer cannot be imaged. Because of their small concentration, these molecules might diffuse as a 2D molecular gas on top of the first layer, but the STM is too slow to image them. The occasional “spikes” in the topography support this hypothesis: Each time a molecule in the second layer diffuses through the tunneling gap, the associated increase of the tunneling current is counteracted by a small temporary retraction of the tip. Because of the high mobility of the molecules at room temperature, these intermittent events lead to “spikes” in the topographic images obtained in constant current mode.^{28–30}

Figure 4 shows an STM image with molecular resolution of the monolayer of quinacridone prepared at room temperature. From this kind of image we are able to extract the spacing between neighboring rows of molecules to be $b = (2.03 \pm 0.02)\text{ nm}$. The indicated error corresponds to the standard deviation of the mean value and does not include any systematic error due to, e.g., a poorly calibrated scanner. For the latter, a relative error of 5% was estimated and has to be added to the statistical error. Within each stack, the molecules are oriented parallel to each other and approximately perpendicular to the row direction. The so-determined unit cell would be a primitive one with orthogonal unit cell vectors. The distance between adjacent molecules within the same stack is about $a = (0.70 \pm 0.01)\text{ nm}$. This value is in good agreement with the spacing of

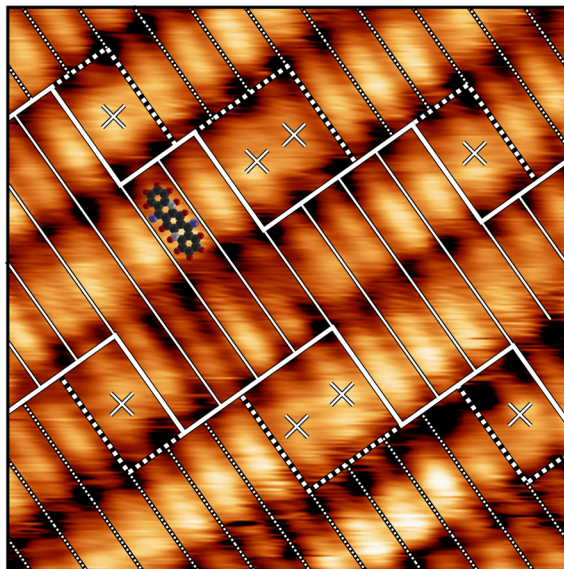


Figure 4. STM image of a molecularly resolved monolayer of quinacridone on Ag(111) at room temperature. The displayed area is $10 \times 10 \text{ nm}^2$. The STM was operated with a bias voltage of $U = 0.5 \text{ V}$ and a current set point of $I = 5 \text{ pA}$. The thin (solid and dashed) lines mark the distance between molecules with a regular spacing. The domain boundaries are labeled by bold (solid and dashed) lines. The molecules at the domain boundaries are labeled by “ \times ” and form spacings that are 1.5 times wider than the regular ones.

hydrogen-bonded quinacridone molecules along the molecular rows in the α or β polymorphs. The same value is also reported by Trixler and co-workers for the spacing between parallel quinacridone molecules within the quinacridone “nanowires” on HOPG fabricated by solid–solid wetting.³¹

Extracting the spacing between adjacent molecules is not as straightforward as it looks. As can be seen in the overview image in Figure 3, the bright parts (stacks) along the molecular rows are separated by short darker sections (defects). To avoid systematic errors, we have extracted the intermolecular distance only from molecules located within the same stacks. At higher magnification, the details of the molecular arrangement can be resolved. An example is shown in Figure 4 together with a network of solid and dotted lines highlighting the positions and relative arrangement of the quinacridone molecules. The crosses mark the “defects” separating stacks of quinacridone along the molecular rows. Thick solid or dashed lines enclose stacks in neighboring rows where the molecules are in perfect registry parallel and perpendicular to the row direction. These different sets of domains (solid and dashed lines), however, form two antiphase domains with a lateral shift of half a lattice spacing along the row direction. The antiphase boundaries are introduced by the “defects” between the stacks or domains and are thus enclosed partly by solid and dotted thick lines. The defects contain either one or two quinacridone molecules (marked by crosses in Figure 4) which appear more “fuzzy” than those in the neighboring stacks. Clearly, each defect introduces a “phase shift” of π (half a unit cell) between the adjacent stacks along the row direction. The apparently regular arrangement of the defects in Figure 4 is accidental: a statistical analysis of the larger scale images (see Figure 3) reveals that the spacing between two defects along the rows follows a random distribution, characterized by an exponentially decaying pair

distribution function with a mean spacing (stack width) of about 4–5 molecules.

An explanation of the structures as revealed by STM involves both the hydrogen bonding and the 2D-chirality of the quinacridone molecules and is illustrated by the model in Figure 5. The tendency to aggregate in stacks of parallel

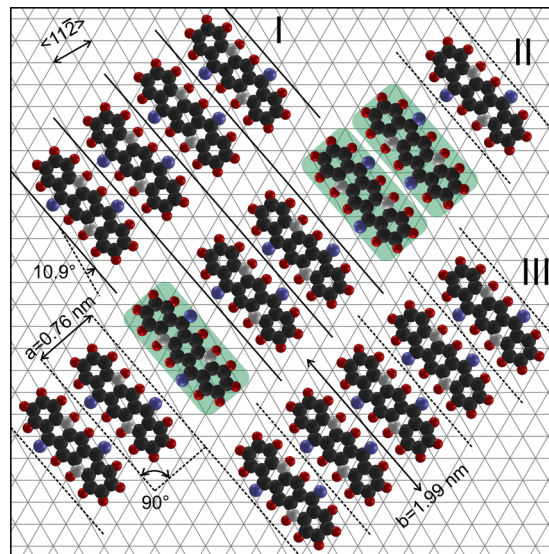


Figure 5. Structure model of the quinacridone monolayer on Ag(111) as deposited at room temperature. The hexagonal mesh represents the Ag(111) lattice. At each intersection of the gray lines a Ag atom is located. The solid and dotted lines separate neighboring quinacridone molecules as in the overlay in the STM image of Figure 4. While the molecules in the stacks all have the same handedness, a minority of the molecules with the “wrong” handedness forms defects which introduce antiphase domains with a phase shift corresponding to half an intermolecular spacing along the row direction.

molecules with an intermolecular spacing of about 0.7 nm can be attributed to the strong interaction mediated by two $\text{C}=\text{O}\cdots\text{H}-\text{N}$ hydrogen bonds between neighboring molecules with the same handedness in a row. The same bonding motif is also dominating the α and β polymorphs in the bulk. On the other hand, the azimuthal orientation of the molecules on the substrate, and, hence, the (perpendicular) orientation of the molecular rows, is determined by the interaction of the quinacridone molecules with the Ag(111) substrate, i.e., the corrugation of the molecule–substrate potential. As mentioned in the Introduction (see Figure 1), quinacridone molecules with different azimuthal orientation can be associated with different 2D-enantiomers, albeit our room temperature STM data do not allow to determine the handedness, directly. Consequently, the two mirror domains composed of rows of molecules oriented $+11^\circ$ and -11° with respect to the $\text{Ag}(11\bar{2})$ direction (see Figure 3) can be attributed to two almost enantiopure phases with opposite handedness. The “defects” in Figure 4 could thus be due to a residual amount (of about 18%) of molecules with the “wrong” handedness, which were trapped during the growth and coalescence of the enantiopure stacks. As can be noticed in Figure 4, molecules in stacks on neighboring rows can have only two possible relative alignments: They are either aligned (in-phase) or shifted by half a unit cell spacing. The existence of only two antiphase domains along the rows suggests that the structure of the quinacridone domains is commensurate along this direction.

In fact, the above growth scenario is very similar to the one observed for indigo on Cu(111) by Villagomez et al.¹³ In this case, the azimuthal orientation of the isolated indigo enantiomers is inclined by about +20° and -20° with respect to the Cu<1 $\bar{1}0$ > direction, respectively. Upon 2D condensation, the indigo molecules were found to self-assemble into mirror domains composed of essentially enantiopure molecular rows oriented +9.5° and -9.5° with respect to the <1 $\bar{1}0$ > direction. After deposition at room temperature, “defects” were also observed along the rows which could be identified as indigo molecules with the “wrong” handedness. These defects could be eliminated almost completely by annealing the sample at 100 °C for 1 h. With their low-temperature STM Villagomez et al., the authors could actually determine the 2D-chirality from the asymmetry of the shape of the STM image for each individual indigo enantiomer.

In order to further quantify the superstructure of the quinacridone adlayer and to explore its suspected commensurability, low-energy electron diffraction (LEED) experiments were performed. Figure 6a shows the characteristic LEED

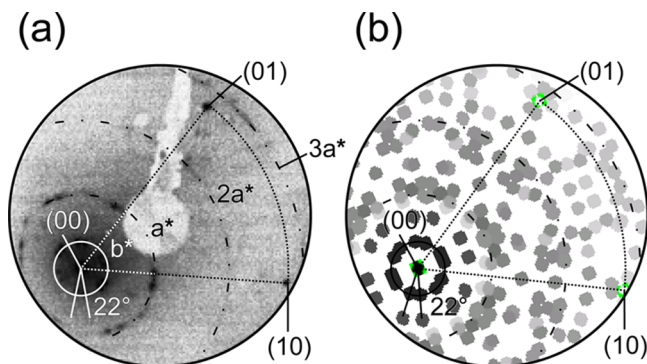


Figure 6. (a) LEED pattern of a monolayer of quinacridone deposited on the Ag(111) surface at room temperature. The LEED pattern was acquired with an electron energy of 30 eV. The sample was intentionally misaligned so that the electron gun did not hide the diffraction spots around the (00) diffraction beam. (b) Simulated LEED pattern on the basis of the superstructure given by the matrix in eq 1.

pattern obtained from the same sample which was previously characterized by STM (see Figures 3 and 4). A major problem with LEED is that very low electron beam energies have to be used to acquire diffraction patterns of large organic molecules with correspondingly large unit cells. These slow electrons can interact very efficiently with the molecules, so that the risk of beam damage is very high. For the particular system of quinacridone on silver, the LEED pattern was only visible for a couple of seconds before it faded away. Therefore, we had to change the position of the sample right before acquisition of a single LEED pattern. In addition, we did not align the sample in the usual way so that the (00) spot is back-reflected into the electron gun. Because of this intentional misalignment, we were able to image the diffraction spots in close proximity to the specular (00) spot, but it also resulted in a geometrical distortion of the diffraction pattern.

Besides the (00) spot, the (10) and the (01) spot of the silver substrate can be identified in the LEED pattern in Figure 6a. This allows determining the symmetry axes of the substrate, i.e., the <11 $\bar{2}$ > directions (indicated by the dotted lines in Figure 6) and calibrating the scale of the observed pattern. The

diffraction pattern of the quinacridone monolayer exhibits a 6-fold symmetry. The most prominent features induced by the quinacridone adlayer are the two rings centered around the (00) spot with radii a^* and b^* . The inner ring consists of 12 individual spots. These 12 spots form six pairs which are azimuthally centered in the middle of the 60° sector defined by the (00), (10), and (01) substrate peaks; i.e., each pair is split symmetrically around the <1 $\bar{1}0$ > direction of the substrate. The radius b^* of the inner ring corresponds to a distance $b = (2.00 \pm 0.17)$ nm in real space, which exactly matches the spacing between neighboring rows of quinacridone molecules (see Figures 3 and 4). As in the following, the experimental error was always estimated from the width of the diffraction spots. Any distortion of the pattern, which is obviously present in Figure 6a, is neglected. In agreement with the STM findings concerning the relative orientations of the different rows of molecules (Figure 3), the splitting between the two spots forming a pair with respect to the <1 $\bar{1}0$ > direction is about 20°–25°. This is fully consistent with the STM observation showing molecular rows with an inclination of ±11° with respect to the <11 $\bar{2}$ > direction.

The second ring with radius a^* , marked with a dash-dotted line in Figure 6, also consists of $2 \times 6 = 12$ intense spots, but their azimuthal position is rotated by 90° with respect to the inner ring. In addition, six additional very faint spots are located just slightly outside this ring. The radius a^* of the second ring can be attributed to the measured spacing a between neighboring molecules in a close-packed stack. Here we find a real space value of $a = (0.72 \pm 0.05)$ nm. Upon closer inspection of the LEED pattern in Figure 6a, one can identify rather diffuse rings with radii $2a^*$ and $3a^*$ which are concentric around the central (00) spot. An important detail for the structural analysis is that the ring with radius $3a^*$ does not intersect the first-order diffraction spots of the substrate but has a radius which is about 7% larger than the length of the {10} reciprocal lattice vectors of the substrate. Taking into account the so-derived values for a and b , the orientation with respect to the symmetry directions of the substrate as well as the commensurability along the a -direction one arrives at a superstructure unit cell which can be expressed in matrix notation as

$$\begin{pmatrix} 3 & 2 \\ -1.5 & 6 \end{pmatrix} \text{ and } \begin{pmatrix} 3 & 1 \\ 1.5 & 7.5 \end{pmatrix} \quad (1)$$

for the two mirror domains, respectively. The half integer values in the second row (i.e., along the b -direction) suggest that the superstructure is actually “high-order commensurate” with a commensurate coincidence lattice with twice the lattice constant b and two inequivalent quinacridone molecules within the commensurate supercell. The primitive unit cell given by eq 1 is also the basis for the model drawn in Figure 5. Within each close-packed stack all the molecules have the same orientation and, therefore, the same handedness on the surface. The fact that there are two antiphase domains with a relative shift of $a/2$ along the row direction and that no Moiré pattern was observed in the STM images is consistent with a simple commensurability of the structure along the a -direction; i.e., all the molecules within the stacks are located on equivalent adsorption sites on the Ag(111) surface. For the model depicted in Figure 5 we assumed that the center of the molecule is located above a 2-fold bridge position of the substrate. In this case, also the two outer aromatic rings are

located very close to bridge sites. Moreover, the molecules in different antiphase domains and in neighboring rows would also rest on bridge sites, albeit nonequivalent ones. A similar arrangement, in which all the molecules are located on a single type of lattice sites, cannot be achieved with on-top or hollow sites. Although this might be a good argument in favor of this particular adsorption geometry, the experimental data do not allow to determine the absolute positions of the molecules.

The matrix is rather speculative for the *b* direction (i.e., the second row of the superstructure matrix) as neither STM nor the LEED measurements at low electron energies are free of distortions. However, in the case of more complicated modes of epitaxy like point-on-line or point-on-point structures,³² Moiré patterns are usually observed in the STM images, which can help to track down the structure. In our case, we did not observe such long-range modulations. Moreover, changing the values of the bottom row of the matrix, i.e., (−1.5, 6) or (1.5, 7.5), by ±10% (which is an upper limit for the experimental uncertainty) would fundamentally change the symmetry of the unit cell, which would then be no longer perfectly rectangular. In addition, the arguments concerning a possible single adsorption site for all quinacridone molecules would no longer be valid.

Although there is a good general agreement concerning the main features and symmetries between the simulated and the measured LEED pattern (see Figure 6a), the simulation predicts many more spots. To make the simulation more accurate, the structure factor of the quinacridone molecule has to be taken into account, rather than a pointlike scattering center. In addition, the STM data show that the periodicity along the rows is quite often interrupted by “defects” introducing antiphase boundaries between consecutive stacks of molecules. For a realistic description of the experimental LEED pattern, the simulation should include these antiphase boundaries and their stochastic distribution.

Quinacridone Monolayer after Heating. The structural properties of a quinacridone monolayer adsorbed on the Ag(111) surface change completely if the sample is heated up to 550 K. This temperature corresponds to the one used in the evaporator during the preparation of the quinacridone thin film. Therefore, we assume that excess molecules in the second and higher layers gain enough thermal energy so that they can desorb from the sample, whereas the quinacridone molecules in the first monolayer in direct contact with the Ag(111) substrate remain on the surface. Indeed, it is quite common that the desorption of the molecules in the first monolayer of an organic film desorb at significantly higher temperatures than those in the multilayer.³³ One can take advantage of this effect to prepare well-defined molecular monolayers: At first, several layers of the organic molecule are deposited, and subsequently all but the first molecular layer are desorbed by heating the sample appropriately. In the present case, quinacridone monolayers which were prepared by depositing a single layer of molecules and subsequently heated (see Figure 9a) and those which were prepared by multilayer desorption (see Figures 7 and 8) exhibit the same structure.

It is surprising that the thermally treated samples have a completely different structure (see Figures 7 and 8) as compared to those deposited at room temperature without further heating (see Figure 3). The domains are often larger than 50 nm in both lateral dimensions although the structures may also be interrupted by discommensuration lines as seen, for instance, in Figure 8. Accordingly, the LEED pattern shown

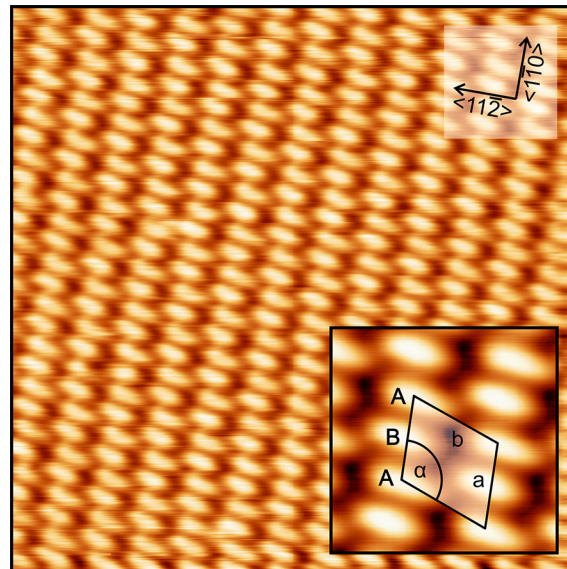


Figure 7. STM image of a quinacridone monolayer on Ag(111), prepared by multilayer desorption: A thick film was deposited while the sample surface was held at room temperature. After deposition, the temperature of the sample was raised up to about 570 K, and then the heating was stopped. The aim of this procedure was to desorb all molecules in excess of one monolayer. The stacking direction of the molecules now coincides with the $\langle 1\bar{1}0 \rangle$ symmetry axis of the substrate. The image has a size of $20 \times 20 \text{ nm}^2$ and was acquired with a bias voltage of $U = -300 \text{ mV}$ and a constant tunneling current of $I = 30 \text{ pA}$. The inset shows an averaged pattern obtained with the “Auto Mesh Average” algorithm of the WSxM software¹⁷ from an STM image similar to the one shown here. The image of the insets represents an area of $4 \times 4 \text{ nm}^2$.

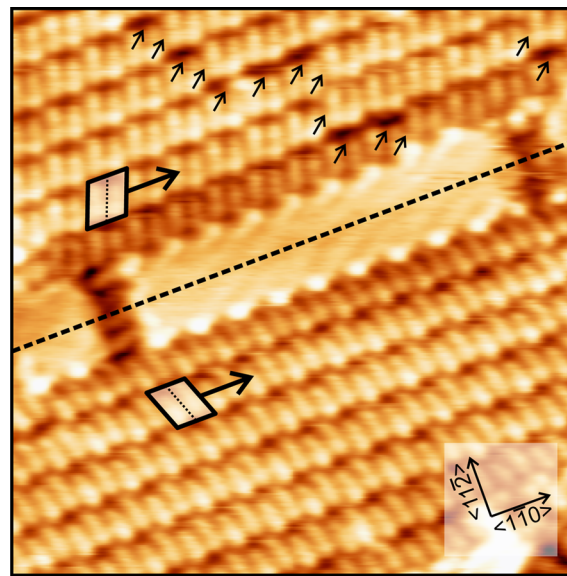


Figure 8. STM image of a quinacridone monolayer on Ag(111) prepared by multilayer desorption (see text and Figure 7). The image has a size of $20 \times 20 \text{ nm}^2$ and was acquired with a bias voltage of $U = -1.0 \text{ V}$ and a current set point of $I = 25 \text{ pA}$. The unit cells of two mirror symmetric domains are indicated in the image. The mirror axis (dashed line) is parallel to the row direction (thick arrows) and coincides with the $\langle 1\bar{1}0 \rangle$ -direction of the substrate. The series of small arrows marks a discommensuration line.

in Figure 9a exhibits much sharper spots than the nonannealed samples (Figure 6a). The STM images in Figures 7 and 8 reveal rows of parallelly stacked quinacridone molecules. The row direction now coincides with the $\langle 1\bar{1}0 \rangle$ symmetry axis of the substrate. While in the nonannealed case all molecules were uniformly aligned along the rows (A–A stacking), the molecules in the annealed monolayer exhibit a kind of A–B stacking. Depending on the resolution of the STM tip (and the tunneling parameters), we can recognize two inequivalent molecules (A and B in Figure 7). Along the molecular rows (a -direction), the molecules are alternately shifted left (A) and right (B) in the direction of the b -axis of the unit cell indicated in Figure 7. The STM image in Figure 8 further reveals that there are two possible, mirror symmetric arrangements of the molecules for a given row direction, since the orientation of the b -axis is not perpendicular to the row direction.

We measured the distance between equivalent molecules, i.e., from one “A” molecule to the next “A” molecule along the row direction, to be $a = (1.46 \pm 0.01)$ nm. The distance between adjacent “A” and “B” molecules is just half of this value, namely 0.73 nm, consistent with the width of a single quinacridone molecule. For the spacing between equivalent molecules in neighboring rows, we find a value of $b = (1.69 \pm 0.01)$ nm. The angle between the two unit cell vectors \vec{a} and \vec{b} is $\alpha = (110 \pm 1)^\circ$ (see inset in Figure 7). Because of the dimer stacking “AB–AB”, the unit cell is no longer primitive but contains at least two molecules. Finally, all the molecules seem to be aligned along the b -direction. In fact, a closer inspection of Figure 8 reveals that the orientation of the molecules in the two mirror domains differs by $(44 \pm 2)^\circ$. Therefore, the long axis of the molecules is rotated by $([90 + 22] \pm 2)^\circ = (112 \pm 2)^\circ$ with respect to the direction of the rows, which coincides with the b -direction within the experimental error.

The LEED pattern of an annealed quinacridone monolayer is shown in Figure 9a. The pattern looks much simpler than the one of the as-prepared surface (see Figure 6a). The inner structure around the (00) spot is just a simple hexagon. The distance b^* of these six spots nearest to the (00) spot corresponds to a distance in real space of $b = (1.66 \pm 0.22)$ nm,

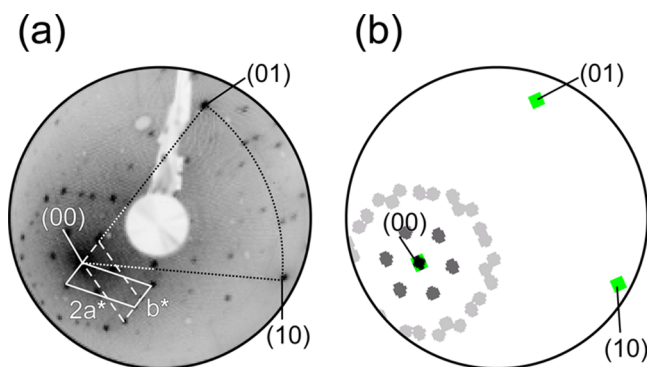


Figure 9. (a) LEED pattern of quinacridone on Ag(111) after deposition of slightly more than one monolayer at room temperature and subsequent annealing at 550 K. The LEED pattern was acquired with an electron energy of 30 eV. The sample is intentionally misaligned so that the electron gun does not hide the diffraction spots around the (00) beam. (b) Corresponding simulated LEED pattern. The simulation is based on the commensurate unit cells given in eq 2 and takes into account the 6-fold symmetry of the substrate. The kinematic simulation assumes point scatterers at the centers of the molecules.

which agrees well with the value for the spacing between neighboring rows as extracted from the STM images. In addition, the six spots are located on the $\langle 11\bar{2} \rangle$ symmetry axes of the substrate. This confirms that the rows are aligned along the $\langle 1\bar{1}0 \rangle$ -directions of the substrate because this arrangement gives rise to a periodicity b along the orthogonal $\langle 11\bar{2} \rangle$ -directions in the diffraction pattern.

Outside the inner hexagon a second, more complicated one is observed. It consists of 12 bright and 12 faint spots. The faint spots on the sides of this hexagon occur in pairs centered around the $\langle 1\bar{1}0 \rangle$ -directions at a distance $2a^*$ from the (00) spot, which corresponds to a spacing of $a/2 = (0.74 \pm 0.04)$ nm. Within the experimental error this value is identical to the spacing between neighboring A and B molecules as deduced from the STM images in Figure 7. The two spots in each pair are split azimuthally by $2\text{--}3^\circ$ with respect to the $\langle 1\bar{1}0 \rangle$ symmetry axes of the substrate. The LEED pattern can be explained by a reciprocal unit cell and its mirror image indicated by the solid and dashed lines in Figure 9, respectively. In total, there are six possible configurations for the unit cell: three rotationally equivalent domains for each of the two mirror symmetric superstructures. Transformation into real space yields the two characteristic matrices

$$\begin{pmatrix} 5 & 5 \\ -1 & 5 \end{pmatrix} \text{ and } \begin{pmatrix} 5 & 5 \\ -5 & 1 \end{pmatrix} \quad (2)$$

for the two mirror domains. These suggested unit cells are also the basis of the kinematic LEED simulations shown in Figure 9b, which are in very good agreement with the measured LEED pattern in Figure 9a.

Note that the first-order superstructure spot $(10)_s$ along the a^* direction (and all other odd multiples) are absent in the LEED pattern, such that only every other spot with a spacing of $2a^*$ can be seen. This is due to the fact that the superstructure unit cell is not a primitive one but contains a second molecule at a position $\vec{a}/2 + \epsilon\vec{b}$, i.e., halfway along the molecular rows and shifted by a fraction ϵ along the b -axis. As a result, the structure factor (which is included in the kinematic simulations) leads to an extinction of all the odd-numbered diffraction spots along the a^* -axis, independent of the relative shift ϵ . However, other (off-axis) diffraction spots containing an odd multiple of a^* , like the $(11)_s$ spot, may have a nonvanishing intensity depending on the value of ϵ . In fact, the kinematic structure factor for the $(11)_s$ spot varies as $\sin^2(\pi\epsilon)$. This means that the $(11)_s$ spot is fully extinct for a perfectly uniform stacking ($\epsilon = 0$) but acquires maximum intensity for a centered $c(2 \times 2)$ type arrangement ($\epsilon = 1/2$). In the latter case, the odd-numbered spots along the b^* -axis would carry zero intensity. Since the $(11)_s$ spot (which is located next to a $(01)_s$ spot of another rotational domain) could not be detected with a measurable intensity and since the $(01)_s$ spot is very bright, we can conclude that the relative shift ϵ along the b -axis between molecules A and B in the unit cell is closer to 0 than to 0.5. Because of the different appearance of the two inequivalent molecules A and B in the STM images (see Figure 7), their relative shift ϵ is hard to judge but should be in the range between 0.1 and 0.2, in accordance with the LEED simulation.

On the basis of the experimental findings, we propose a structure model for the annealed quinacridone monolayer on Ag(111), which is illustrated in Figure 10. The model is based on the unit cells in eq 2 with two flat-lying molecules aligned

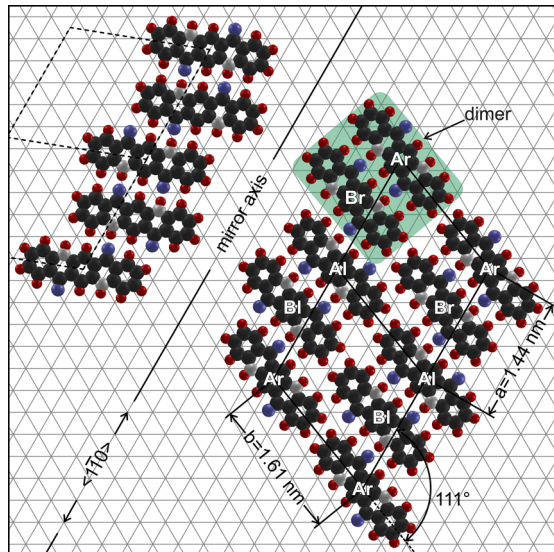


Figure 10. Model of the annealed monolayer of quinacridone on Ag(111) as described in the text. At each intersection of the gray lines a Ag atom is located. The solid line marks the superstructure unit cell according to eq 3. The unit cell of mirror symmetric domain is indicated by dashed lines. The mirror axis coincides with the $\langle 1\bar{1}0 \rangle$ -axis of the substrate. The labeling of the molecules accounts for the inequivalent sites in the unit cell ("A" and "B") and the different 2D-handedness of the molecules on the surface ("r" and "l").

along the b -axis and shifted by a certain fraction ϵ along this axis. In order to arrange the molecules within the unit cell, we tried to optimize the number of hydrogen bonds, especially those between the oxygen and the NH group of adjacent molecules. In doing so, we realized that the periodic indentation of the molecules along the rows is incompatible with enantiopure stacking. This would rather lead to uniform, quasi-one-dimensional rows oriented perpendicular to the molecular long axis, as observed in the nonannealed monolayer phase (see Figure 5). Likewise, stacking molecules with alternating handedness would also favor straight rows of molecules but with their long axis inclined against the direction normal to the rows. In fact, the periodic indentation together with the observed inclination of the molecules can best be accounted for by a combination of the two limiting cases, i.e., a sequence of homochiral dimers with alternating handedness. As a result, a stacking of the type "Ar–Br–Al–Bl" as shown in Figure 10 is obtained where "A" and "B" refer to the two inequivalent lattice sites and "r" (right) and "l" (left) denote the two different 2D-chiral enantiomers. We want to emphasize that (i) we have no experimental proof for this peculiar stacking sequence, apart from the intuitive arguments concerning the lateral interaction strength, and (ii) we do not know the exact position and orientation of the two molecules within the unit cell, except that the molecules should be (nearly) parallel and aligned, within a few degrees, along the b -axis ($\pm 9^\circ$ with respect to the nearest $\langle \bar{1}10 \rangle$ axis of the substrate). The biggest uncertainty is the amount of the offset along the b -axis between molecules A and B. Varying this parameter (ϵ), we can make the stacking such that the hydrogen bonds between neighboring molecules either form straight lines (as chosen in Figure 10) or zigzag chains across the molecules. Clearly, submolecularly resolved STM images and/or theoretical calculations are needed to clarify these points.

A direct consequence of the suggested "Ar–Br–Al–Bl" stacking is that the actual periodicity along the rows (a -direction) is increased by a factor of 2, so that the actual superstructure unit cells taking into account the 2D-chirality of the molecules should be given by

$$\begin{pmatrix} 10 & 10 \\ -1 & 5 \end{pmatrix} \text{ and } \begin{pmatrix} 10 & 10 \\ -5 & 1 \end{pmatrix} \quad (3)$$

for the two mirror domains. Each unit cell thus contains four molecules (two enantiomers with opposite handedness for each of the two sites A and B). The fact that neither the STM images nor the LEED patterns are sensitive to the doubling of the periodicity from a to $2a$ along the molecular rows is easily explained: the doubling of the periodicity is solely due to the different handedness of adjacent quinacridone dimers. Our STM studies were conducted at room temperature, and the images do not allow to resolve the fine contrast between different enantiomers. As far as the LEED measurements are concerned, the atom factors for the backscattering of 30 eV electrons for the elements carbon, nitrogen, and oxygen are almost the same,³⁴ while the contribution of the hydrogen atoms can be totally neglected. In addition, the symmetry of the quinacridone molecules reduces the effect of the 2D-chirality even further: The contribution to the molecular structure factor of 18 carbon atoms, which do not change their relative positions upon mirroring the quinacridone molecule along its long axis, clearly outweigh the contribution of the two carbon, two oxygen, and two nitrogen atoms, which actually exchange positions. Therefore, the diffraction contrast between the two enantiomers of the quinacridone molecules adsorbed on the surface is likely too small to provide enough intensity at the half-integer positions along the a^* -direction in the LEED pattern.

Comparison between the Quinacridone Structures.

The structures of the first layer of quinacridone can best be compared to the α^1 phase discussed by Paulus and co-workers in ref 9. Table 1 shows our data vis-à-vis the $(\bar{1}\bar{1}1)$ plane of this

Table 1. Comparison between the Suggested Superstructures of Monolayer Quinacridone (QA) on Ag(111) and the $(\bar{1}\bar{1}2)$ Plane of the α^1 Polymorph⁹*

	Z	a (nm)	b (nm)	\angle (deg)	mol area A (nm 2)
QA/Ag(111) as-prepared	1	0.70	2.03	90.0	1.421
QA/Ag(111) annealed	4	4·0.72	1.61	111.1	1.084
$(\bar{1}\bar{1}2)$ plane of α^1 -QA ⁹	1	0.69	1.69	110.3	1.092

*Z represents the number of molecules per unit cell given by the length of the vectors $a = |\vec{a}|$ and $b = |\vec{b}|$ and the angle (\angle) between the two. The final column contains the calculated area per molecule, i.e., $A = \cos \angle \cdot ab/Z$.

bulk polymorph. Only the α^1 polymorph exhibits a primitive unit cell. For the other polymorphs, the unit cell contains two molecules which are tilted with respect to each other. In the γ polymorphs, each molecule interacts with four of its neighbors via hydrogen bonds in a nonplanar geometry. In the case of the α^1 and the β polymorph, two hydrogen bonds connect adjacent molecules and form rows of parallel molecules. Neighboring molecular rows do not share the same plane but are tilted or vertically shifted, depending on the crystal plane that is used to cut through the crystal. A rather flat configuration is obtained

for the low index $(\bar{1}\bar{1}2)$ plane of the α^1 polymorph. Therefore, we compare the quasi-two-dimensional monolayer structures of quinacridone on Ag(111) with this particular plane.

For the as-prepared and the annealed monolayer of quinacridone on Ag(111), an intermolecular spacing of about 0.7 nm is found along the stacking direction. This is quite similar to the distance between adjacent molecules along the $[110]$ direction of the α^1 polymorph, which amounts to 0.69 nm. Along this direction parallel aligned molecules form hydrogen bonded stacks and can thus maximize their binding energy.

Whereas also the direction and the length of the second unit cell vector \vec{b} of the annealed phase matches almost perfectly the values of projected bulk unit cell, there are significant differences between the as-prepared structure of quinacridone and its α^1 polymorph. As quantified in Table 1, the annealed monolayer of quinacridone is considerably denser than the as-prepared monolayer at room temperature. In the early stage of deposition, the substrate surface will impose a particular adsorption geometry (with a mirror symmetric orientation for the two 2D-chiral enantiomers). Other quinacridone molecules will preferentially attach via strong hydrogen bonds in a parallel configuration, thus forming straight enantiopure stacks which assemble into extended domains of molecular rows. These rows are held together by weaker van der Waals interactions. Although the packing density in the nonannealed phase is rather low, this structure is stable for days. Therefore, it is likely that the energy barrier required to initiate the transition from the nonannealed phase into the more densely packed heterochiral phase is considerably higher than the thermal energy available at room temperature. In fact, the temperature required to trigger the transformation is only slightly lower than the sublimation temperature of the α^1 quinacridone bulk phase. This makes sense if one considers that the transition from the homochiral phase into the heterochiral phase upon annealing requires the breaking of the strong hydrogen bonds between molecules originally arranged in homochiral stacks.

SUMMARY AND CONCLUSIONS

The growth and the monolayer stuctures of quinacridone on Ag(111) were investigated by PEEM, STM, and LEED. The quinacridone molecule is prochiral, since it acquires a handedness when adsorbed flat on a surface. For room temperature deposition a $(\begin{smallmatrix} 3 & 2 \\ -1.5 & 6 \end{smallmatrix})$ superstructure and its mirror domains are obtained. The structure is characterized by stacks of quinacridone molecules of a few nanometers length, which assemble into quasi-one-dimensional molecular rows. The individual stacks and the row direction is oriented at $+10.9^\circ$ and -10.9° with respect to the $\langle 11\bar{2} \rangle$ symmetry axis of the Ag(111) surface. The perpendicular orientation of the molecules in the stacks and along the rows is a strong indication that these are composed of molecules with the same handedness. The stacks are separated by “defects” (probably molecules with the “wrong” handedness), which introduce a large number of antiphase boundaries.

Upon annealing at high temperature, the monolayer structure changes completely. From the STM and LEED data a well-ordered $(\begin{smallmatrix} 5 & 5 \\ -1 & 5 \end{smallmatrix})$ superstructure, containing two molecules per unit cell, and its mirror image are inferred. In the annealed phase the quinacridone molecules also form extended rows, but the molecules are no longer oriented

perpendicular to the row direction. In addition, every second molecule is shifted along the b -axis of the superstructure unit cell, such that rows are periodically indented. This geometry cannot be explained by a simple enantiopure stacking. Instead, we propose a stacking sequence of homochiral pairs of molecules with alternating handedness. Taking this heterochiral ordering into account would double the periodicity along the rows (a -direction), leading to a $(\begin{smallmatrix} 10 & 10 \\ -1 & 5 \end{smallmatrix})$ superstructure (with four atoms per unit cell) and the corresponding mirror image.

The observed monolayer structures are the result of two competing effects: (i) the interaction between the quinacridone molecules, in particular, the strong hydrogen bonds connecting neighboring molecules in the stacks, and (ii) the 2D-chirality of the adsorbed quinacridone molecules which determines the arrangement of the molecules within these stacks. As a result, two very distinct structures can be stabilized on the Ag(111) surface for which the particular stacking sequence is intimately linked with the different chiral ordering. Finally, the interaction between the quinacridone molecules and the Ag(111) surface is responsible for the flat-lying geometry of the molecules as well as the particular epitaxial relationships of the monolayer structures, namely the specific orientations of the molecular rows and the commensurability of the superstructures.

In order to transform the (metastable) nonannealed homochiral phase into the denser heterochiral phase, the former has to be annealed at very high temperature, as the chiral reordering requires the breaking of the strong hydrogen bonds.

ASSOCIATED CONTENT

Supporting Information

Movie showing the growth sequence which was also used to extract the data depicted in Figure 2; the original length of the movie is 23 min 24 s; for the reason for the file size the image resolution was decreased and the frame rate was adapted. This material is available free of charge via the Internet at <http://pubs.acs.org>.

AUTHOR INFORMATION

Corresponding Author

*E-mail thorsten.wagner@jku.at; Ph +43 (0)732 2468 8505; Fax +43 (0)732 2468 8509 (T.W.).

Notes

The authors declare no competing financial interest.

ACKNOWLEDGMENTS

This work is financially supported by the Austrian Science Fund (FWF) under project No. P24528-N20. The authors want to acknowledge the fruitful discussion about the thin film growth of quinacridone on copper surfaces with Prof. Roland Resel and Michael Pachler from the Technical University Graz. We want to thank Prof. Rolf Möller, University Duisburg-Essen, for his assistance with the LEEDsim software.

REFERENCES

- (1) Glowacki, E. D.; Irimia-Vladu, M.; Kaltenbrunner, M.; Gsiorowski, J.; White, M. S.; Monkowius, U.; Romanazzi, G.; Suranna, G. P.; Mastrolilli, P.; Sekitani, T.; et al. Hydrogen-Bonded Semiconducting Pigments for Air-Stable Field-Effect Transistors. *Adv. Mater.* **2013**, *25*, 1563–1569.
- (2) Glowacki, E. D.; Leonat, L.; Irimia-Vladu, M.; Schwödiauer, R.; Ullah, M.; Sitter, H.; Bauer, S.; Sariciftci, N. S. Intermolecular

- Hydrogen-Bonded Organic Semiconductors - Quinacridone versus Pentacene. *Appl. Phys. Lett.* **2012**, *101*, 023305(4pp).
- (3) Glowacki, E. D.; Leonat, L.; Voss, G.; Bodea, M.; Bozkurt, Z.; Irimia-Vladu, M.; Bauer, S.; Sariciftci, N. S. Natural and Nature-Inspired Semiconductors for Organic Electronics. *Proc. SPIE* **2011**, *8118*, 81180M .
- (4) Labana, S. S.; Labana, L. L. Quinacridones. *Chem. Rev.* **1967**, *67*, 1–18.
- (5) Zollinger, H. *Color Chemistry: Syntheses, Properties, and Applications of Organic Dyes and Pigments*; Wiley-VCH: Weinheim, 2003.
- (6) Faulkner, E. B., Schwartz, R. J., Eds.; *High Performance Pigments*; Wiley-VCH: Weinheim, 2009.
- (7) Potts, G. D.; Jones, W.; Bullock, J. F.; Andrews, S. J.; Maginn, S. J. The Crystal Structure of Quinacridone: An Archetypal Pigment. *J. Chem. Soc., Chem. Commun.* **1994**, *94*, 2565–2566.
- (8) Panina, N.; Leusen, F. J. J.; Janssen, F. F. B. J.; Verwer, P.; Meekes, H.; Vlieg, E.; Deroover, G. Crystal Structure Prediction of Organic Pigments: Quinacridone as an Example. *J. Appl. Crystallogr.* **2007**, *40*, 105–114.
- (9) Paulus, E. F.; Leusen, F. J. J.; Schmidt, M. U. Crystal Structures of Quinacridones. *CrystEngComm* **2007**, *9*, 131–143.
- (10) Gao, H.-Z. Theoretical Study on Charge Transport of Quinacridone Polymorphs. *Int. J. Quantum Chem.* **2012**, *112*, 740–746.
- (11) Koller, G.; Berkebile, S.; Ivano, J.; Netzer, F.; Ramsey, M. Device Relevant Organic Films and Interfaces: A Surface Science Approach. *Surf. Sci.* **2007**, *601*, S683–S689.
- (12) Barth, J. V.; Weckesser, J.; Trimarchi, G.; Vladimirova, M.; De Vita, A.; Cai, C.; Brune, H.; Günter, P.; Kern, K. Stereochemical Effects in Supramolecular Self-Assembly at Surfaces: 1-D versus 2-D Enantiomeric Ordering for PVBA and PEBA on Ag(111). *J. Am. Chem. Soc.* **2002**, *124*, 7991–8000, PMID: 12095343.
- (13) Villagomez, C. J.; Guillermet, O.; Goudeau, S.; Ample, F.; Xu, H.; Coudret, C.; Bouju, X.; Zambelli, T.; Gauthier, S. Self-Assembly of Enantiopure Domains: The Case of Indigo on Cu(111). *J. Chem. Phys.* **2010**, *132*, 074705(8pp).
- (14) Raval, R. Chiral Expression from Molecular Assemblies at Metal Surfaces: Insights from Surface Science Techniques. *Chem. Soc. Rev.* **2009**, *38*, 707–721.
- (15) Ernst, K.-H. Molecular Chirality at Surfaces. *Phys. Status Solidi B* **2012**, *249*, 2057–2088.
- (16) Nečas, D.; Klapetek, P. Gwyddion: An Open-Source Software for SPM Data Analysis. *Cent. Eur. J. Phys.* **2012**, *10*, 181–188, DOI: 10.2478/s11534-011-0096-2.
- (17) Horcas, I.; Fernandez, R.; Gomez-Rodriguez, J. M.; Colchero, J.; Gomez-Herrero, J.; Baro, A. M. WSXM: A Software for Scanning Probe Microscopy and a Tool for Nanotechnology. *Rev. Sci. Instrum.* **2007**, *78*, 013705(8pp).
- (18) Wagner, T.; Fritz, D. R.; Zeppenfeld, P. Probing Organic Nanostructures by Photoelectron-Emission Microscopy. *Appl. Surf. Sci.* **2013**, *267*, 26–29 .
- (19) Wagner, T.; Fritz, D. R.; Zeppenfeld, P. Standing and Flat Lying α -6T Molecules Probed by Imaging Photoelectron Spectroscopy. *Org. Electron.* **2011**, *12*, 442–446.
- (20) Fleming, A. J.; Netzer, F. P.; Ramsey, M. G. Nucleation and 3D Growth of Para-Sexiphenyl Nanostructures from an Oriented 2D Liquid Layer Investigated by Photoemission Electron Microscopy. *J. Phys.: Condens. Matter* **2009**, *21*, 445003(11pp).
- (21) Fleming, A. J.; Berkebile, S.; Ules, T.; Ramsey, M. G. Pre-Nucleation Dynamics of Organic Molecule Self-Assembly Investigated by PEEM. *Phys. Chem. Chem. Phys.* **2011**, *13*, 4693–4708.
- (22) Marchetto, H.; Groh, U.; Schmidt, T.; Fink, R.; Freund, H.-J.; Umbach, E. Influence of Substrate Morphology on Organic Layer Growth: PTCDA on Ag(111). *Chem. Phys.* **2006**, *325*, 178–184 .
- (23) Michaelson, H. B. The Work Function of the Elements and its Periodicity. *J. Appl. Phys.* **1977**, *48*, 4729–4733.
- (24) Chelvayohhan, M.; Mee, C. Work Function Measurements on (110), (100) and (111) Surfaces of Silver. *J. Phys.: Condens. Matter* **1982**, *15*, 2305–2312.
- (25) Li, W. Y.; Goto, K.; Shimizu, R. PEEM is a Suitable Tool for Absolute Work Function Measurements. *Surf. Interface Anal.* **2005**, *37*, 244–247.
- (26) Ishii, H.; Sugiyama, K.; Ito, E.; Seki, K. Energy Level Alignment and Interfacial Electronic Structures at Organic/Metal and Organic/Organic Interfaces. *Adv. Mater.* **1999**, *11*, 605–625.
- (27) Ivano, J. Intrinsic Work Function of Molecular Films. *Thin Solid Films* **2012**, *520*, 3975–3986.
- (28) Ikonomov, J.; Bach, P.; Merkel, R.; Sokolowski, M. Surface Diffusion Constants of Large Organic Molecules Determined from their Residence Times under a Scanning Tunneling Microscope Tip. *Phys. Rev. B* **2010**, *81*, 161412(4pp).
- (29) Sloan, P. A. Time-Resolved Scanning Tunnelling Microscopy for Molecular Science. *J. Phys.: Condens. Matter* **2010**, *22*, 264001(8pp).
- (30) Liu, Q.; Wang, K.-d.; Xiao, X.-d. Surface Dynamics Studied by Time-Dependent Tunneling Current. *Front. Phys. China* **2010**, *5*, 357–368.
- (31) Trixler, F.; Markert, T.; Lackinger, M.; Jamitzky, F.; Heckl, W. M. Supramolecular Self-Assembly Initiated by Solid-Solid Wetting. *Chem.—Eur. J.* **2007**, *13*, 7785–7790.
- (32) Hooks, D. E.; Fritz, T.; Ward, M. D. Epitaxy and Molecular Organization on Solid Substrates. *Adv. Mater.* **2001**, *13*, 227–241.
- (33) Wagner, T.; Karacuban, H.; Möller, R. Analysis of Complex Thermal Desorption Spectra: PTCDA on Copper. *Surf. Sci.* **2009**, *603*, 482–490.
- (34) Henry, R. J. W.; Burke, P. G.; Sinfailam, A.-L. Scattering of Electrons by C, N, O, N⁺, O⁺, and O⁺². *Phys. Rev.* **1969**, *178*, 218–225.